Ultrasound–fluoroscopy registration for prostate brachytherapy dosimetry

Ehsan Dehghan [a,b], Junghoon Lee [a,c], Pascal Fallavollita [d], Nathanael Kuo [e], Anton Deguet [f], Yi Le [c], E. Clif Burdette [g], Danny Y. Song [c], Jerry L. Prince [a], Gabor Fichtinger [b,*]

[a] Department of Electrical and Computer Engineering, Johns Hopkins University, Baltimore, MD, USA
[b] School of Computing, Queen's University, Kingston, ON, Canada
[c] Department of Radiation Oncology and Molecular Radiation Sciences, Johns Hopkins University, School of Medicine, Baltimore, MD, USA
[d] Chair for Computer Aided Medical Procedures & Augmented Reality, Technische Universität München, Germany
[e] Department of Biomedical Engineering, Johns Hopkins University, Baltimore, MD, USA
[f] Department of Computer Science, Johns Hopkins University, Baltimore, MD, USA
[g] Acoustic MedSystems Inc., Champaign, IL, USA

ARTICLE INFO

ABSTRACT

Prostate brachytherapy is a treatment for prostate cancer using radioactive seeds that are permanently implanted in the prostate. The treatment success depends on adequate coverage of the target gland with a therapeutic dose, while sparing the surrounding tissue. Since seed implantation is performed under transrectal ultrasound (TRUS) imaging, intraoperative localization of the seeds in ultrasound can provide physicians with dynamic dose assessment and plan modification. However, since all the seeds cannot be seen in the ultrasound images, registration between ultrasound and fluoroscopy is a practical solution for intraoperative dosimetry. In this manuscript, we introduce a new image-based nonrigid registration method that obviates the need for manual seed segmentation in TRUS images and compensates for the prostate displacement and deformation due to TRUS probe pressure. First, we filter the ultrasound images for subsequent registration using thresholding and Gaussian blurring. Second, a computationally efficient point-to-volume similarity metric, an affine transformation and an evolutionary optimizer are used in the registration loop. A phantom study showed final registration errors of 0.84 ± 0.45 mm compared to ground truth. In a study on data from 10 patients, the registration algorithm showed overall seed-to-seed errors of 1.7 ± 1.0 mm and 1.5 ± 0.9 mm for rigid and nonrigid registration methods, respectively, performed in approximately 30 s per patient.

1. Introduction

With an estimated number of 240,890 new cases in 2011, prostate cancer is the most common cancer among men in the United States, accounting for 29% of their cancers (Siegel et al., 2011). It is also the second highest cause of cancer death among men in the United States (Siegel et al., 2011). Radical prostatectomy, external-beam radiation therapy and brachytherapy are established treatments for prostate cancer. Low-dose-rate brachytherapy (hereafter, brachytherapy) is an effective and minimally invasive treatment for localized prostate cancer that can achieve outcomes at least equal to the other treatment options while showing less severe side-effects (Merrick et al., 2001; Blasko et al., 2002; Morris et al., 2009). In brachytherapy, the cancer is eradicated by internal radiation from permanently implanted radio-active sources (seeds) of ^{125}I, ^{103}Pd, or ^{137}Cs. Generally, the physician implants 40–130 seeds using needles, based on the size of the prostate and the type and activity of the seeds. Before the operation, the seed positions are planned using a transrectal ultrasound (TRUS) volume. The goal of the planning is to cover the target gland with a prescribed dose of radiation, while sparing the healthy surrounding tissue such as urethra and rectum. In contemporary brachytherapy, seed placement is performed under visual guidance from TRUS.

In practice, the actual delivered implant geometry is different from the plan for several reasons including intraoperative tissue swelling (Yamada et al., 2003), prostate motion and deformation caused by needle insertion (Lagerburg et al., 2005), needle deflection (Nath et al., 2000) and seed migration. Deviation of the seeds from their planned positions results in a sub-optimal dose distribution. Over-radiation of the healthy surrounding tissue may lead to

* Corresponding author. Address: School of Computing, Queen's University, 557 Goodwin Hall, Kingston, ON, Canada K7L 3N6. Tel.: +1 613 533 3258; fax: +1 613 533 6513.

E-mail addresses: ehsand@jhu.edu (E. Dehghan), junghoon@jhu.edu (J. Lee), fallavol@in.tum.de (P. Fallavollita), nkuo8@jhmi.edu (N. Kuo), anton.deguet@jhu.edu (A. Deguet), yle1@jhmi.edu (Y. Le), clifb@acousticmed.com (E.C. Burdette), dsong2@jhmi.edu (D.Y. Song), prince@jhu.edu (J.L. Prince), gabor@cs.queensu.ca (G. Fichtinger).

complications such as sexual and urinary dysfunction, and rectal ulceration. Excessive under-radiation of the cancerous gland may result in treatment failure. Traditionally, the delivered dose is quantitatively assessed using CT after the patient is released from the operating room.

Dynamic dosimetry—the ability to calculate the delivered dose intraoperatively, based on the actual position of the implanted seeds—enables the physician to adjust the plan and ensure sufficient dose coverage before the completion of the operation. Moreover, a dynamic dosimetry system may render postimplant CT-based dose evaluation unnecessary, as the delivered dose can be quantitatively assessed at the end of the operation. This will significantly reduce brachytherapy quality assurance complexity and cost.

In order to have accurate intraoperative dosimetry, one should be able to localize the deposited seeds in relation to the prostate. A variety of methods have been tried to localize the seeds in ultrasound images (Han et al., 2003; Holmes and Robb, 2004; Feleppa et al., 2002; McAleavey et al., 2003; Mitri et al., 2004; Ding et al., 2006; Xue et al., 2005; Wei et al., 2006; Wen et al., 2010). However, US-only seed localization is not considered a reliable tool for dose calculation as this method suffers from missing seeds in ultrasound images and presence of false positives—seed-like artifacts caused by calcification and air bubbles (Han et al., 2003).

An alternative technique used in brachytherapy treatment and available by commercialized products entails estimation of the seed positions based on the position of the needle visible in sagittal images. This method was further refined so that the seeds are manually localized in sagittal ultrasound images at the time of deposition (Potters et al., 2003; Meijer et al., 2006; Nag et al., 2001; Polo et al., 2010). Although this method showed improvements in the treatment outcome (Nath et al., 2009; Nag et al., 2001), it cannot account for intraoperative seed displacement after implantation caused by edema, tissue motion and/or seed migration.

The secondary imaging modality often utilized in brachytherapy operating rooms is C-arm fluoroscopy, which is more reliable than TRUS for seed visualization. However, a C-arm image shows a 2D projection of the implant geometry with no soft-tissue detail. Nonetheless, brachytherapists frequently use C-arm images for gross implant evaluation based on their mental 3D visualization of the seeds.

Although C-arm images do not have sufficient soft-tissue contrast to show the prostate boundaries, three or more C-arm images can be used to reconstruct the seeds in 3D (Amols and Rosen, 1981; Su et al., 2004; Narayanan et al., 2004; Lam et al., 2004; Jain et al., 2005b; Brunet-Benkhoucha et al., 2009; Lee et al., 2009, 2011b,a; Dehghan et al., 2011a,c). The seeds reconstructed from C-arm images can be registered to the prostate delineated in TRUS images to calculate the delivered dose. Therefore, ultrasound–fluoroscopy fusion can provide a practical solution for dynamic dosimetry and has demonstrated its benefits in limited clinical trials (Orio et al., 2007; Song et al., 2011).

Registration of the reconstructed seeds to the TRUS coordinate system is a necessary step for ultrasound–fluoroscopy fusion and has been extensively studied (Todor et al., 2003; Jain et al., 2012; Song et al., 2011; French et al., 2005; Su et al., 2007b; Orio et al., 2007; Tutar et al., 2008; Fallavollita et al., 2010; Dehghan et al., 2011b). Lead markers on the TRUS probe or radio-opaque fiducials were used for ultrasound–fluoroscopy registration (Todor et al., 2003; Jain et al., 2012). French et al. (French et al., 2005) used the probe as a fiducial for ultrasound–fluoroscopy registration.

In order to avoid image occlusion by the probe, it is necessary to retract the probe, at least partially, before the C-arm image acquisition. Since the physicians usually press the probe against the prostate to achieve a good acoustic coupling and improve the TRUS image quality, probe retraction results in prostate motion in the posterior direction and sometimes deformation (Wallner et al., 2001). The marker- and fiducial-based registration methods cannot account for this motion and deformation.

As a remedy, Su et al. (2007b), Orio et al. (2007) and Tutar et al. (2008) used a point-to-point registration method between ultrasound and fluoroscopy. In this method, the physician manually localizes some seeds in the sagittal TRUS images. This point set is then registered to the seeds reconstructed from the C-arm images. Manual seed localization in TRUS images is a difficult and time-consuming task and is entirely dependent on accurate seeds determined, rather subjectively, by the physician. Therefore, registration methods that rely on manual seed segmentation are not appropriate for wide-scale practical implementation.

Fallavollita et al. were the first to propose an intensity-based registration between CT or fluoroscopy and TRUS (Fallavollita et al., 2010). They reported successful registration results between CT and TRUS on a ground truth phantom. They also reported qualitative agreement between TRUS and fluoroscopy for a single patient data set. Since a rigid registration method was used in (Su et al., 2007b; Orio et al., 2007; Tutar et al., 2007, 2008; Fallavollita et al., 2010), they could only account for rigid motion of the prostate due to probe retraction but not for the likely deformation.

For a more comprehensive review on intraoperative imaging and dosimetry techniques for prostate brachytherapy, we refer the readers to (Polo et al., 2010).

Despite considerable research and development efforts, dynamic dosimetry is not yet available for clinical use in brachytherapy (Nath et al., 2009). A practical method for TRUS-fluoroscopy fusion is a much sought-after solution to surmount the last standing obstacle in the road toward dynamic dosimetry.

In this paper, we introduce a new image-based TRUS-fluoroscopy registration algorithm. Our method obviates the need for manual seed segmentation in TRUS images and is robust to missing seeds and false positives in the TRUS images. In addition, by employing a deformation model based on the observed nature of the probe-prostate interaction, our algorithm is capable of compensating for the effects of prostate motion and deformation caused by probe retraction. To the best of our knowledge, this is the first nonrigid registration method for TRUS-fluoroscopy fusion for prostate brachytherapy.

We employ thresholding to prepare the TRUS images for registration, without any attempt to remove the false positives or identify the missing seeds. We also apply Gaussian blurring to increase the capture range of our registration method that exploits a robust evolutionary optimizer (Hansen, 2006). We examined our algorithm on a phantom and on patient data. In addition to excellent visual agreement, our registration method shows errors that are smaller than clinically acceptable levels (customarily, less than 2 mm). We also examined our registration method in prediction of dose parameters compared to CT-based dosimetry. Since rapid computations are essential for practical dynamic dosimetry, our method runs in approximately 30 s per patient. With fast and accurate C-arm-based seed reconstruction methods available (Lee et al., 2011b,a; Dehghan et al., 2011a,c), our algorithm can be readily integrated into a practical system to provide dynamic dosimetry for prostate brachytherapy in clinical application.

Compared to the work of Fallavollita et al. (2010), we introduce a deformable registration method that compensates for the effects of probe pressure. Our method also shows lower registration errors and faster computational speed. In addition, we use different pre-processing steps, similarity metric and optimizer to enhance the robustness of our algorithm. The underlying idea of our method for a rigid registration was presented in (Dehghan et al., 2011b). This manuscript significantly extends our previous work by presenting a deformable registration method, and by providing a more

detailed description of the methodology and performance analysis on 10 clinical data sets.

This paper is organized as follows: In Section 2 we discuss the components of the registration algorithm and explain the experimental method on phantom and clinical data sets. The results are presented in Section 3, followed by the discussions in Section 4. At the end, conclusions and the future work are outlined in Section 5.

2. Materials and method

2.1. Workflow

We envision the following workflow for providing intraoperative dosimetry analysis and optimization using ultrasound–fluoroscopy registration. At some point during the operation or immediately at the end, the physician acquires a series of transverse TRUS images of the prostate by continuously retracting the probe from the prostate base toward its apex (see Fig. 1a). Since some of the seeds may be located superior to the base or inferior to the apex, it is recommended that the whole range be covered during image acquisition. These slices are concatenated into a volume that is used for registration (Fig. 1b). After acquiring TRUS images, the physician fully retracts the probe. Then several C-arm images are taken from different angles (Fig. 1c). These images are processed for distortion correction and seed segmentation (Kuo et al., 2012). The seeds are reconstructed in 3D space from the processed C-arm images (Fig. 1d) and are registered to the TRUS volume (Fig. 1e). After registration, the dose distribution is calculated and the isodose contours are overlaid on the TRUS images. At this stage, the under-dosed regions (cold spots) or the regions with high risk of over-radiation can be detected. The physician can change the planned position of the remaining seeds and add new seeds, if necessary, to compensate for possible errors.

2.2. TRUS image preprocessing

In order to prepare the TRUS image volume for registration, we apply the following preprocessing steps. First, a region of interest is selected by the user to confine the search region for optimization and to increase the robustness of the algorithm. The region of interest is selected from a transverse slice of the mid-gland, by marking the two corners of a rectangle that encloses the prostate. A volume of interest (VOI) is generated by cropping the same region in the other slices and compounding them. As preoperative prostate contours are usually available from the TRUS volume, the region of interest can be defined automatically using the contours of the prostate gland.

The reconstructed seeds from C-arm images have no information about soft tissue. However, ultrasound usually provides a low contrast image of soft tissue variations. Although the reconstructed seeds and the TRUS volume do not seem to be appropriate for an image-based registration, implantation of the metallic seeds inside the prostate changes the TRUS images advantageously. The implanted seeds cause strong reflections in the ultrasound beam that appear as bright regions in the TRUS images. These bright regions can be used to establish a correlation between the ultrasound volume and the reconstructed seed cloud. Although calcifications and air bubbles trapped in the needle tracks produce bright regions too, most of the bright regions are caused by the seeds. Based on this intuition, the reconstructed seeds can be registered to the TRUS coordinate system using the intensity of the TRUS images. Since we correspond the bright regions to the seeds, thresholding the ultrasound images can enhance seed visibility. Therefore, we produce a thresholded image I_T from the VOI such that:

$$I_{\mathrm{T}}(x,y,z) = \begin{cases} 0 & \text{if } I(x,y,z) < \mu_{\mathrm{u}} + \alpha\sigma_{\mathrm{u}} \\ 1 & \text{if } I(x,y,z) \geq \mu_{\mathrm{u}} + \alpha\sigma_{\mathrm{u}} \end{cases} \tag{1}$$

In this equation $I(\cdot)$ is the image intensity at a given position, μ_{u} and σ_{u} are the mean and standard deviation of image intensity in the
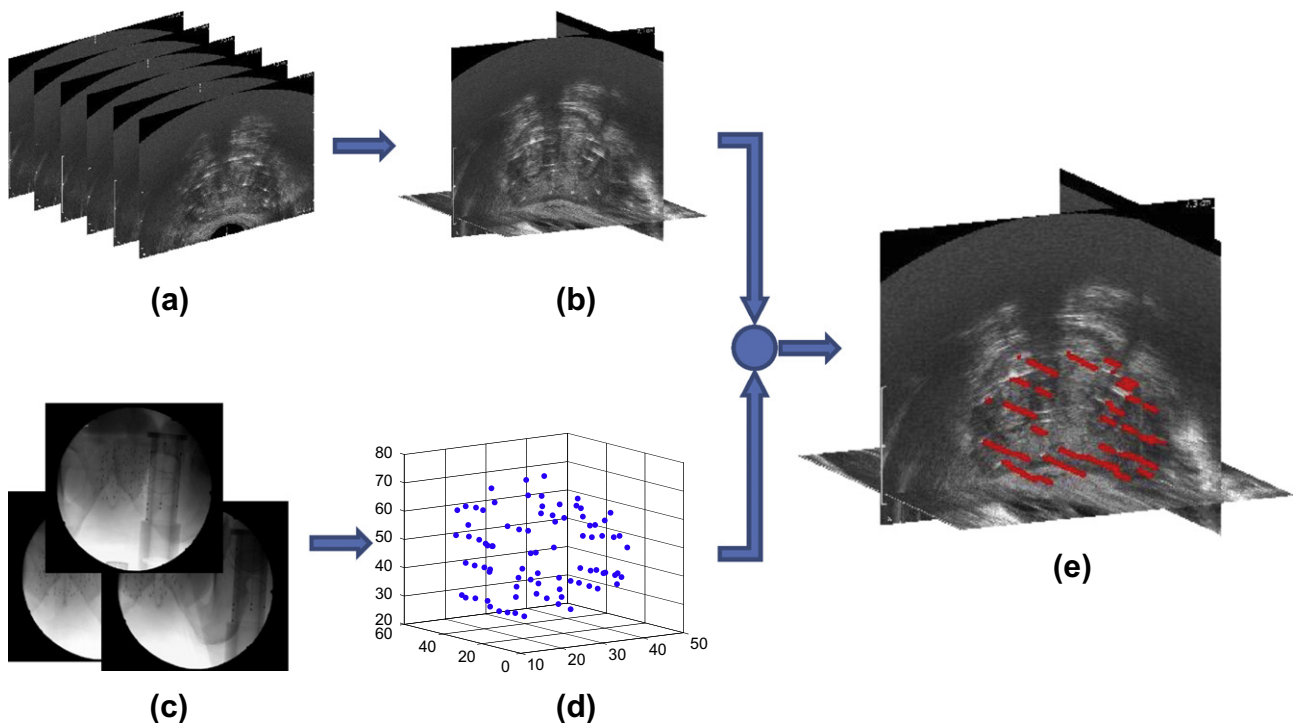
Fig. 1. The workflow for ultrasound–fluoroscopy registration. (a): Several transverse images of the prostate. (b): A volume created from the slices. (c): Several C-arm images taken from different angles. (d): Seeds reconstructed in 3D. (e): Registered seeds overlaid on the US volume. Seeds are shown as capsules.

VOI, respectively, and α is a threshold parameter (We will discuss this parameter in more detail in Section 3.4). A mid-gland slice of the VOI before and after thresholding is shown in Fig. 2a and b, respectively.

After thresholding, we apply an Euclidean distance transform to each slice of the VOI and produce a distance map image (I_D) according to the following equation.

$$I_D(x,y,z) = \min_{x_s,y_s} \sqrt{(x - x_s)^2 + (y - y_s)^2}, \qquad (2)$$
$$\text{s.t. } I_T(x_s, y_s, z) = 1.$$

The distance transform defines the value of each pixel in I_D as the minimum Euclidean distance from that pixel to the nearest white pixel in the same slice of I_T (i.e. the distance to the closest seed candidate). Fig. 2c shows the result of the distance transform applied to Fig. 2b.

Finally, a Gaussian function is applied to the distance map image to produce a Gaussian-blurred image (I_G) such that:

$$I_G(x,y,z) = \exp\left(-\frac{I_D^2(x,y,z)}{2\sigma^2}\right), \qquad (3)$$

where, I_G is the volume of interest after Gaussian blurring and σ is the standard deviation of the Gaussian function. Fig. 2d shows the effect of the Gaussian function applied to Fig. 2c. The Gaussian-blurred volume is used as a target volume in the registration loop.

2.3. Point-to-volume registration

In this section, we describe an image-based affine registration method to register the reconstructed seeds to the preprocessed VOI. Since transformation of a set of points is computationally more efficient compared to transformation of a volume, we assume that the VOI is fixed and transform the seed cloud.

The probe pressure is mostly in the anterior-posterior (AP) direction and fairly uniform along the long axis of the probe. Therefore, we use a 1D scaling along the AP-axis to account for the prostate deformation caused by the probe pressure. Although this is a slightly simplified model of the prostate deformation, our results in Section 3.2 show that this model is sufficiently accurate for clinically acceptable results.

2.3.1. Transformation

We assume a TRUS coordinate system O_{xyz} such that the x axis is parallel to the horizontal axis of the image from left to right, the y axis is parallel to its vertical axis from bottom to top and the z axis is parallel to the long axis of the probe from the prostate base to its apex. We define an affine transformation $T : \mathbb{R}^3 \to \mathbb{R}^3$ between the C-arm and TRUS coordinate systems such that:

$$T(\mathbf{x}) = \begin{bmatrix} 1 & 0 & 0 \\ 0 & \lambda^{-1} & 0 \\ 0 & 0 & 1 \end{bmatrix} \mathbf{R}(\theta)\mathbf{x} + \mathbf{t}, \qquad (4)$$

where, $\mathbf{x}$ represents the coordinates of any point in the C-arm coordinate system, $\mathbf{R}$ is a rotation matrix, $\theta = [\theta_R, \theta_P, \theta_Y]$ represents the roll, pitch and yaw angles, $\mathbf{t} = [t_x, t_y, t_z]^T$ shows translation along the x, y and z axes, and λ is the scaling along the y axis of the TRUS coordinate system.

We did not scale the seed cloud along the x and z axes, in order to avoid any destructive influence of lower image quality in these two directions on the registration algorithm. Note that ultrasound volume is usually created by stacking several axial slices. Therefore, the resolution along the z axis is low. In addition, seeds that are located at the anterior region of the prostate usually appear as wide (along the x axis) bright regions as US beam is wider in this area.

2.3.2. Similarity metric

The seeds reconstructed from C-arm fluoroscopy images are considered as a set of points. This can be used favorably to formulate a computationally efficient point-to-volume similarity metric. We assume rectangular cuboids of dimensions $\Delta x \times \Delta y \times \Delta z$ around each reconstructed seed in the TRUS coordinate system.
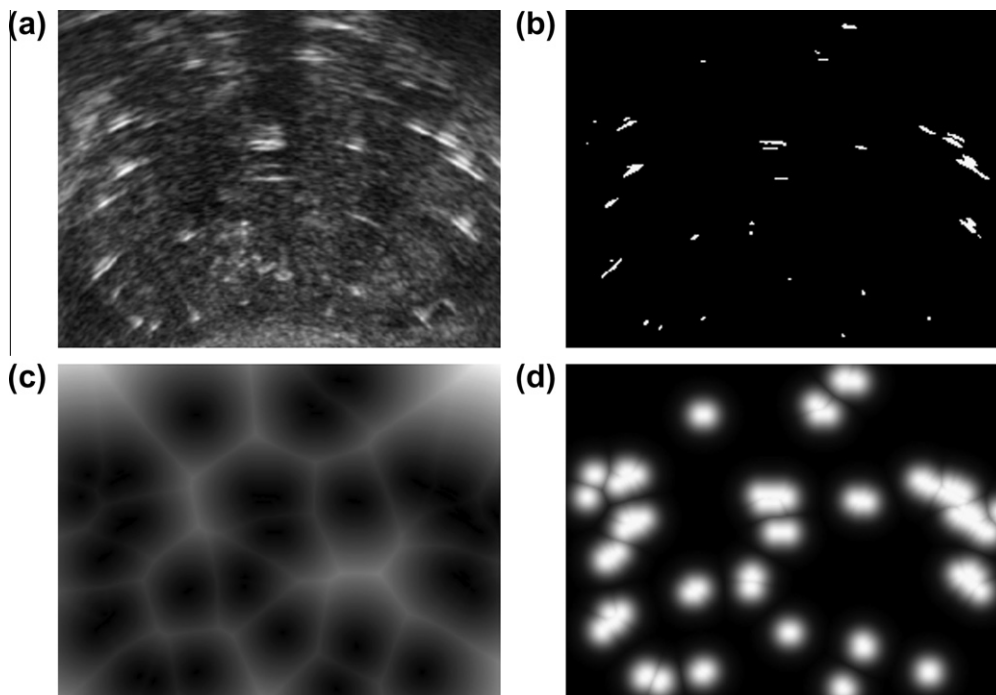

Fig. 2. Preprocessing steps. (a): One slice from VOI. (b): The same slice after thresholding. (c): After application of distance transform. (d): After application of the Gaussian function.

In this work, cuboids of the size $2 \times 2 \times 6 \ mm^3$—slightly thicker and longer than a seed—were used. Our similarity metric is equal to the integral of the image intensity over all the cuboids and hence it quantifies the overlap between the cuboids and the bright regions in the VOI. Therefore:

$$S = \sum_{n=1}^{N} \int_{-\frac{\Delta z}{2}}^{\frac{\Delta z}{2}} \int_{-\frac{\Delta y}{2}}^{\frac{\Delta y}{2}} \int_{-\frac{\Delta x}{2}}^{\frac{\Delta x}{2}} I_G \left(T(\mathbf{s}_n) + \begin{bmatrix} x \\ y \\ z \end{bmatrix} \right) dx \, dy \, dz, \quad (5)$$

where, $\mathbf{s}_n$ represents the coordinates of the nth seed in the C-arm coordinate system. Since the similarity metric in (5) quantifies the overlap between the cuboids and the large bright regions caused by the seeds, it guides the reconstructed seeds toward the centers of the bright regions.

2.3.3. Optimizer

The registration problem can be written as the following constrained optimization problem:

$$(\mathbf{t}^*, \boldsymbol{\theta}^*, \lambda^*) = \arg \max \ S(\mathbf{t}, \boldsymbol{\theta}, \lambda) \quad (6)$$

$$\text{s.t.} \begin{cases} \mathbf{t}_{min} \leqslant \mathbf{t} \leqslant \mathbf{t}_{max} \\ \boldsymbol{\theta}_{min} \leqslant \boldsymbol{\theta} \leqslant \boldsymbol{\theta}_{max} \\ \lambda_{min} \leqslant \lambda \leqslant \lambda_{max}. \end{cases}$$

We employ the Covariance Matrix Adaptation Evolution Strategy (CMA-ES) (Hansen, 2006) to solve the constrained optimization problem in (6). This algorithm is a stochastic method for continuous-domain optimization of nonlinear and nonconvex problems and is known for its robustness and efficiency. CMA-ES samples the search region based on a multivariate normal distribution, the covariance matrix of which is adapted using the information from the sample points at each iteration and information from previous iterations. The sampling and adaptation proceeds iteratively until convergence to the optimal solution.

It should be noted that the thresholded TRUS volume is a sparse binary image. Therefore, if the thresholded volume is used in (5), changes in the optimization parameters may result in insignificant or no change in the similarity metric. However, application of the distance transform and the Gaussian blurring as explained in Section 2.2, spreads the bright regions and produces a smooth and discernible change of intensity in the image. This continuous and smooth intensity change guides the optimization algorithm toward the optimal solution, enlarges its capture range and also improves its convergence. In this work, the standard deviation of the Gaussian filter is chosen so that the output of the filter decreases to 75% at 1 mm away from a white pixel. If the standard deviation is too small, the bright spots are not spread sufficiently to provide a large basin of convergence. If the standard deviation is too large, the white spots are spread widely and this can increase the influence of the false positives.

3. Experiments and results

3.1. Phantom study

We tested our registration algorithm on a CIRS-053 prostate brachytherapy training phantom (CIRS Inc., VA, USA) implanted with 48 dummy seeds.

In order to establish a ground truth, the phantom was imaged using CT. The phantom box was equipped with 6 fiducial beads visible in CT images (see Fig. 3). The seed clusters were segmented in the CT volume by thresholding. The center of mass of the seed clusters were grouped into a set of points similar to the outcome of seed reconstruction from C-arm images. The relationship between
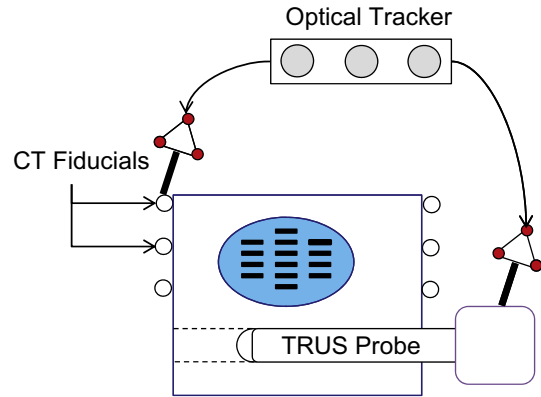
Fig. 3. The ground truth phantom. The registration between CT and TRUS volumes is provided using fiducial markers on the phantom box. Both markers and TRUS probe are tracked using an optical tracker.

the seeds and the beads (manually localized in CT images) provided the seed positions in the phantom coordinate system.

In addition, several transverse slices of TRUS images were acquired during a continuous retraction of the probe and compounded into a volume with pixel spacing of $0.29 \times 0.29 \times 0.35 \ mm^3$. The TRUS probe was tracked using a Cetrus optical tracker (NDI, ON, Canada) and a calibrated pointer (Traxtal Inc., ON, Canada) during imaging with respect to the phantom box fiducial beads (see Fig. 3). The TRUS image coordinate system was registered to the phantom box coordinate system using the method in (Chen et al., 2009). The positions of the CT seeds were transformed to the TRUS coordinate system and were assumed as the ground truth.

We applied independent perturbations of −15 mm to 15 mm with steps of 1 mm along each axis and rotations of −15° to 15° with steps of 1° around each axis to the CT seeds. In order to simulate the effects of missing seeds in the TRUS, we added some seeds to the CT seeds at random positions. We conducted the experiment with a complete CT seed cloud as well as with 5 and 10 extra seeds. Since the added seeds did not have a counterpart in the TRUS volume, they could simulate the effect of missing seeds in the TRUS images. The positions of the added seeds were randomly selected for each value of translational or rotational perturbation.

We also simulated the effect of false positives in the TRUS volume, in another experiment, when some randomly selected seeds were removed from the ground truth seeds. In this case, the experiment was carried out with 5 and 10 seeds removed form the CT seed cloud. Since the images of these seeds in the TRUS volume did not correspond to any seeds in the reduced seed cloud, they acted as false positives in the TRUS volume. The removed seeds were randomly selected for each value of translational or rotational perturbation.

The registration algorithm successfully converged closely to the global optimum (ground truth seed positions) in all the 930 simulations with a maximum average registration error of 1.34 mm. This shows the wide capture range of our algorithm and also its robustness to the missing and false positive seeds. Fig. 4 shows two TRUS images of the phantom marked with the ground truth and registered seeds. Table 1 summarizes the registration results of our phantom study. The seed-to-seed distance between the ground truth seeds and the registered seeds was considered as the registration error. We should emphasize that the range of translational and rotational perturbations applied in this phantom study is larger than the error in the initial guess one may encounter in clinical cases.
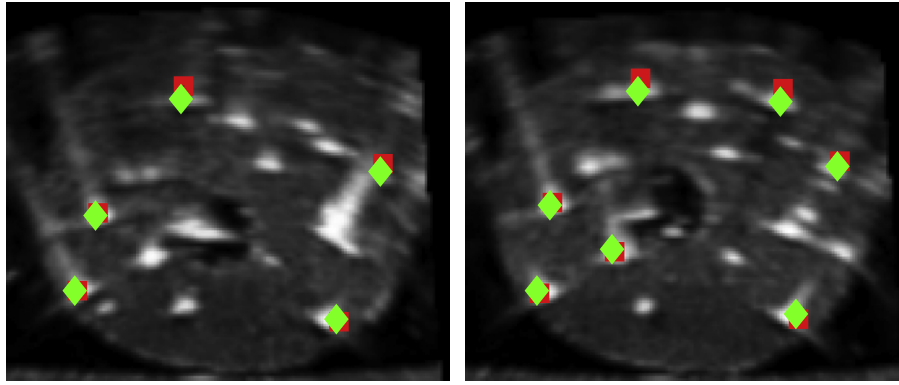
Fig. 4. Two transverse slices of the phantom overlaid with ground truth seeds (squares) and registered seeds (diamonds).

Table 1
Mean and SD of registration error for phantom study.

Seed cloud	Registration error (mm) Mean ± SD (Max)
Complete	0.77 ± 0.40 (1.99)
Missing 5	0.79 ± 0.40 (2.01)
Missing 10	0.84 ± 0.42 (2.18)
Extra 5	0.86 ± 0.46 (3.10)
Extra 10	0.93 ± 0.52 (3.81)
Overall	0.84 ± 0.45

The phantom had a dedicated hole to place the TRUS probe. In addition, care was taken to avoid phantom compression by the probe during TRUS imaging. Although the probe pressure was insignificant, we used affine registration in our phantom study. We assumed $\mathbf{t}_{max} = -\mathbf{t}_{min} = [20,20,20]^T$ (mm), $\theta_{max} = -\theta_{min} = [20°,20°,20°]$ and $1 \leqslant \lambda \leqslant 1.3$ as our constraints in (6).

3.2. Clinical data

We evaluated our algorithm on clinical data sets acquired from 10 patients implanted with 61–105 (median = 78) [103]Pd seeds at the Johns Hopkins Hospital, Baltimore, MD, USA. The physician implanted the seeds using visual feedback from a BK Pro Focus (BK Medical, MA, USA) ultrasound machine.

For ultrasound image acquisition, the physician continuously retracted the TRUS probe from 5–10 mm superior to the base to 5–10 mm inferior of the apex while the images were automatically recorded at 1 mm intervals. The TRUS images had a pixel size of 0.19×0.19 mm[2]. In order to achieve computational speed, we sub-sampled the images after thresholding and Gaussian blurring to create a volume with a voxel size of $0.38 \times 0.38 \times 1.00$ mm[3].

After full retraction of the TRUS probe, we acquired 9 C-arm images in a 20° cone around the AP-axis of the patient using a GE OEC 9600 mobile C-arm (GE Healthcare, WI, USA). A radio-opaque fiducial (Jain et al., 2005a) was mounted on the guiding template for C-arm pose calculation. The C-arm images were processed for geometric distortion correction, seed and fiducial segmentation and pose computation, postoperatively (Kuo et al., 2012). The seeds were reconstructed in 3D space using 5–6 images using a dimensionality reduced linear programming approach with automatic pose correction (called APC-REDMAPS) (Lee et al., 2011a).

We tested our registration algorithm in rigid ($\lambda = 1$) and affine modes. The rotational parameters were initialized by aligning the reconstructed seeds with the planned positions of the seeds using the iterative closest point (ICP) algorithm. The translational param-

eters were initialized so that the center of mass of the reconstructed seeds coincided with the center of the VOI. The scaling parameter for the affine registration was initialized as $\lambda = 1$. For our clinical data sets we used $\mathbf{t}_{max} = -\mathbf{t}_{min} = [15,15,15]^T$ (mm), $\theta_{max} = -\theta_{min} = [15°,15°,15°]$ and $1 \leqslant \lambda \leqslant 1.3$ as our constraints in (6). Since the probe always compresses the prostate, we assume $\lambda \geqslant 1$.

Figure 5 shows several transverse images from mid-gland of 9 patients, overlaid with seeds after affine registration. As it can be seen, there is an excellent visual agreement between the bright spots in the images and the registered seeds. Figure 6 shows two mid-gland images of the prostate for patients 2 and 5, overlaid with seeds resulted from affine and rigid registrations. The true positions of some identifiable seeds are marked with arrows in these figures. As it can be seen, the affine registration method results in a better visual agreement between the real and the registered seeds.

After each registration, the results were visually inspected to assure a successful registration. Since no ground truth for seed positions was available at this stage, we manually selected some seed-like bright spots close to the registered seeds as candidates and carefully examined them in the axial and sagittal slices to make sure they are true seeds. If several seeds were implanted back-to-back, we usually selected the first and last seeds on the row. These bright spots were selected mostly from the posterior region of the prostate where seed visibility was better. Also note that prostate gland deformation is the greatest in this region. Fig. 7 shows a sample of deformably registered and selected seeds for one of the patients. The mean and standard deviation of the seed-to-seed distances between the registered and the centers of the selected seeds are reported in Table 2, as registration error for affine and rigid registrations, for all the patients. The correspondence problem between the selected and registered seeds was solved using the Hungarian algorithm. We tried our best to select the seeds with high confidence. As a result, the number of selected seeds is only 52% of the implanted seeds (See Table 2).

As expected, the affine registration method showed superior performance compared to the rigid registration method in term of seed-to-seed registration error. Table 2 shows that, for all of the patients, the affine registration method resulted in a seed-to-seed registration error of less than 2 mm which is customarily considered as the clinically acceptable threshold.

In order to analyze the error along each axis, the seed-to-seed error vector was projected onto the x, y and z axes. The mean and standard deviation of the absolute value of the projected error along each axis is reported in Table 3. As it can be seen in Table 3, the error along the x and y axes are generally smaller than the error along the z axis, because our TRUS volume had a slice spacing of 1 mm along the z axis. Moreover, it is difficult to accurately localize
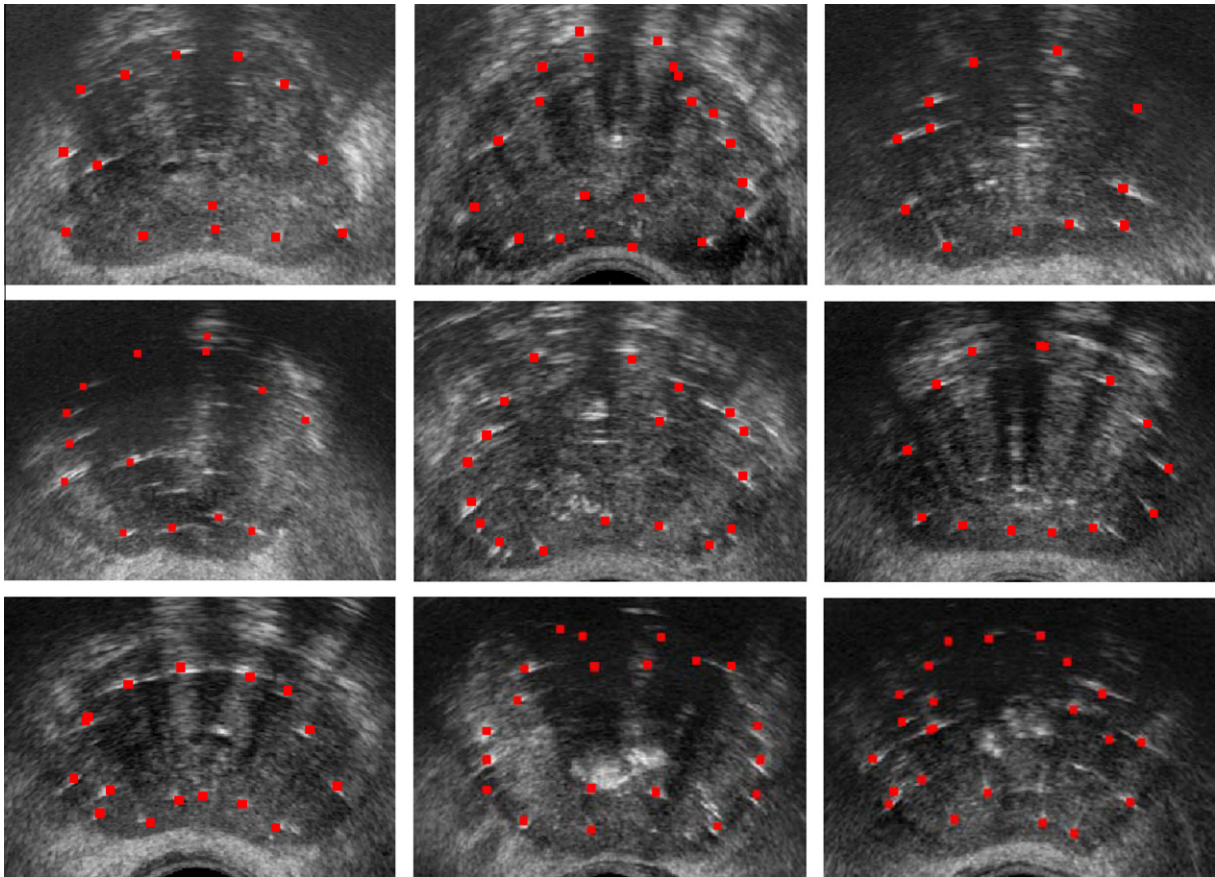
Fig. 5. Clinical results: registered seeds overlaid on mid-gland slices of the prostate for nine patients.
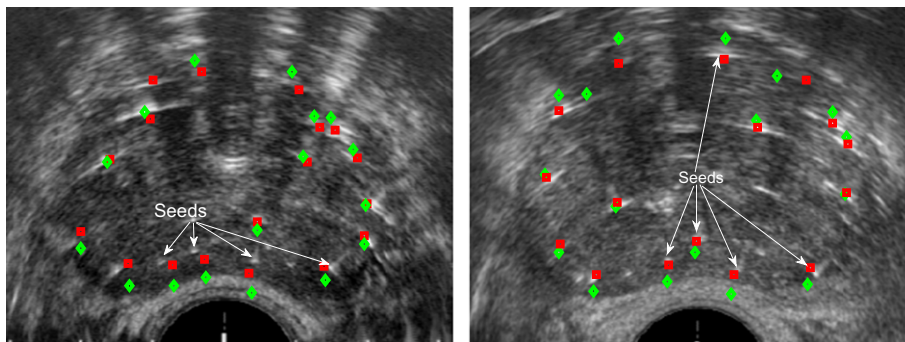

Fig. 6. Two transverse slices from the second (left) and fifth (right) patients, showing the seeds as a result of affine (squares) and rigid (diamonds) registration. The true position of some identifiable seeds are shown with arrows.

the center of each individual seed along the insertion axis if several seeds are implanted back-to-back. Even for single seeds, the uncertainty in the localization of the seed centroid is higher along the z axis, since the seed image is usually elongated due to the needle tracks. The errors caused by the slice spacing and manual segmentation along the z axis contribute to the registration error along this axis.

We also conducted a dosimetry study on 9 of the patients for whom postimplant prostate contours and CT images were available. In order to calculate the delivered dose to the prostate, an experienced radiation oncologist delineated the prostate in the postimplant TRUS and Day-1 CT (acquired one day after the procedure) images. Fig. 8 shows the prostate volume segmented in Day-1 CT and postimplant TRUS. The prostate volume was measured to be 39.0 ± 10.2 cc (Mean ± SD) using Day-1 CT and 38.2 ± 7.6 cc based on postimplant TRUS images. We calculated the delivered dose using the seed positions obtained from rigid and affine ultrasound–fluoroscopy registrations and the postimplant TRUS prostate contours. For comparison, we calculated the delivered dose using seed positions and prostate contours segmented in Day-1 CT as well.

In this work, we computed and reported two important dose parameters—V_{100} and D_{90}. The former is the percentage of the prostate volume covered with 100% of the prescribed dose and the latter is the percentage of the prescribed dose delivered to the 90% of the prostate volume. For dose calculation throughout this work, we approximated the seeds as point sources (Rivard et al., 2004).
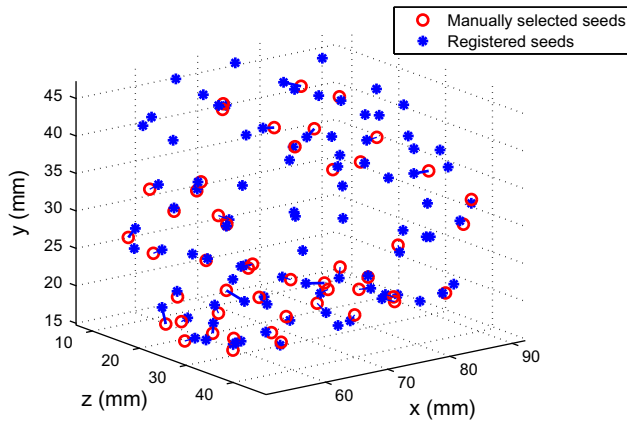
Fig. 7. Deformably registered seeds (blue stars) and manually selected seeds (red circles). (For interpretation of the references to colour in this figure legend, the reader is referred to the web version of this article.)

Fig. 8. Prostate volume segmented in Day-1 CT and postimplant TRUS.

Table 2
Seed-to-seed registration error (Mean ± SD (Max)).

| Patient	Number of seeds		Rigid	Affine	
ID	Total	Selected	Reg. err. (mm)	Reg. err. (mm)	Scale (λ)
1	76	49	1.7 ± 0.7 (4.1)	1.5 ± 0.7 (3.5)	1.09
2	90	56	2.3 ± 1.1 (4.9)	1.7 ± 0.8 (3.8)	1.19
3	64	35	1.6 ± 1.0 (3.9)	1.4 ± 0.8 (3.1)	1.04
4	105	41	1.5 ± 0.6 (3.0)	1.4 ± 0.7 (2.8)	1.08
5	91	49	2.4 ± 1.3 (5.4)	1.6 ± 1.0 (5.1)	1.20
6	73	44	1.9 ± 1.0 (4.2)	1.9 ± 1.1 (5.2)	1.09
7	61	31	1.5 ± 0.8 (3.8)	1.4 ± 0.8 (3.7)	1.04
8	67	38	1.3 ± 0.9 (3.2)	1.1 ± 0.7 (4.0)	1.11
9	102	60	1.4 ± 0.7 (3.6)	1.3 ± 0.8 (3.9)	1.11
10	81	23	1.6 ± 0.8 (4.0)	1.3 ± 0.8 (3.8)	1.12
Overall	810	426	1.7 ± 1.0	1.5 ± 0.9	1.11 ± 0.05

Table 3
Absolute value of projection of seed-to-seed vector along each axis (Mean ± SD).

Patient ID	Absolute projected error (mm)					
	Rigid			Affine		
	x	y	z	x	y	z
1	0.5 ± 0.5	0.7 ± 0.4	1.2 ± 0.8	0.5 ± 0.5	0.4 ± 0.3	1.1 ± 0.8
2	0.7 ± 0.6	1.5 ± 1.1	1.3 ± 0.9	0.7 ± 0.5	0.7 ± 0.7	1.2 ± 0.9
3	0.5 ± 0.4	0.5 ± 0.4	1.4 ± 1.1	0.4 ± 0.4	0.4 ± 0.4	1.1 ± 0.8
4	0.6 ± 0.4	0.7 ± 0.5	0.9 ± 0.7	0.6 ± 0.5	0.5 ± 0.5	0.9 ± 0.8
5	0.4 ± 0.3	1.5 ± 1.1	1.5 ± 1.2	0.4 ± 0.2	0.6 ± 0.4	1.2 ± 1.1
6	0.6 ± 0.6	0.7 ± 0.6	1.3 ± 1.1	0.6 ± 0.6	0.5 ± 0.5	1.5 ± 1.2
7	0.5 ± 0.4	0.6 ± 0.4	1.1 ± 0.8	0.5 ± 0.4	0.4 ± 0.4	1.2 ± 0.8
8	0.3 ± 0.3	0.8 ± 0.8	0.8 ± 0.6	0.4 ± 0.3	0.4 ± 0.4	0.8 ± 0.7
9	0.3 ± 0.3	0.8 ± 0.6	1.0 ± 0.8	0.4 ± 0.3	0.3 ± 0.3	1.1 ± 0.8
10	0.6 ± 0.6	0.8 ± 0.5	1.0 ± 0.7	0.5 ± 0.5	0.5 ± 0.4	0.9 ± 0.7
Overall	0.5 ± 0.4	0.9 ± 0.8	1.1 ± 0.9	0.5 ± 0.4	0.5 ± 0.6	1.1 ± 0.9

Fig. 9 shows the dosimetry parameters calculated using affine and rigid ultrasound–fluoroscopy registrations and Day-1 CT for patients 1–9. Table 4 compares the rigid and affine registration methods in term of their accuracy in prediction of the dose parameters, assuming the Day-1 CT-based parameters as the ground truth. Fig. 9 and Table 4 show the potential of our registration algorithm as an intraoperative and quantitative dose assessment tool that can give the radiation oncologist an opportunity to make implantation adjustments to improve the target coverage.

For each dose parameter in Table 4 we report a prediction error, such that:

$$e_p = |p_{CT} - p_{UF}|, \qquad (7)$$
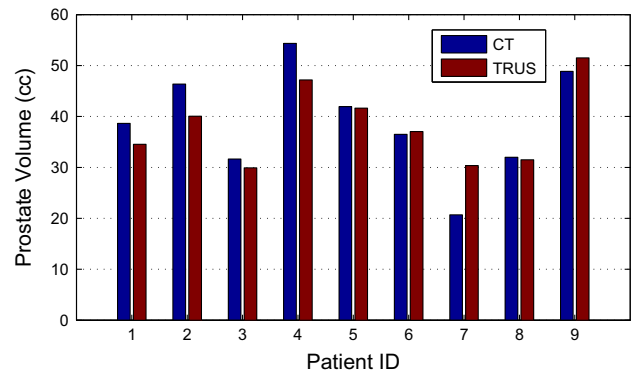
where, e_p is the prediction error for a dose parameter (V_{100} or D_{90}), p_{CT} is the value of that parameter obtained based on Day-1 CT, and p_{UF} is its value calculated using ultrasound–fluoroscopy registration. As it can be seen in Table 4, the affine registration method resulted in an average prediction error of 1.7% for V_{100}, while this error is less than 5% for all of the patients in our study. Such small prediction errors suggest that our ultrasound–fluoroscopy registration method can be used intraoperatively to assure full prostate coverage before the patient is released from the operating room. This in turn, improves the result of postoperative CT dosimetry and reduces the chance that the patient needs to be brought back for additional treatment. In addition, the small dose parameter prediction errors show that manually selected seeds used for validation did not result in significant bias.

3.3. Computational speed

Our algorithm was implemented in MATLAB on a computer with an Intel Core 2 CPU (2 GHz) and 2 GB of RAM. MATLAB implementation of CMA-ES was provided by N. Hansen.[1] The registration time—including preprocessing and manual selection of the region of interest—is approximately 30 s per patient which we consider clinically acceptable. We expect to achieve significantly faster registrations by an optimized implementation of our algorithm in C++ or by using GPU. Since the implementation of the affine registration is not significantly more costly, the affine registration method is more advantageous compared to the rigid registration method, considering its lower seed-to-seed and V_{100} prediction errors.

As mentioned before, preoperative prostate contours are usually available and can be used for automatic selection of the VOI, in order to decrease the runtime and remove the need for manual intervention. As indicated in Section 2.3.3, the search region was limited to ±15 mm along each axis and ±15° around each axis from the initial estimate. This search region was sufficiently large for all the patients. Optimization in a larger search region may require a larger number of function evaluations and hence, more computational time. However, considering the fast speed of our algorithm, registration with a larger search region can be implemented, if necessary, without violating practical temporal performance restrictions.

The maximum number of function evaluations was set to 2500 for the optimization algorithm. This number was conservatively chosen as we achieved successful registration results with smaller number of iterations as well. Although other termination criteria such as a limit on the variation of the optimization parameters or the similarity metric can be used, our termination criterion results in an almost constant computational time for all the patients.

---

[1] Available online at: http://www.lri.fr/hansen/cmaes_inmatlab.html.
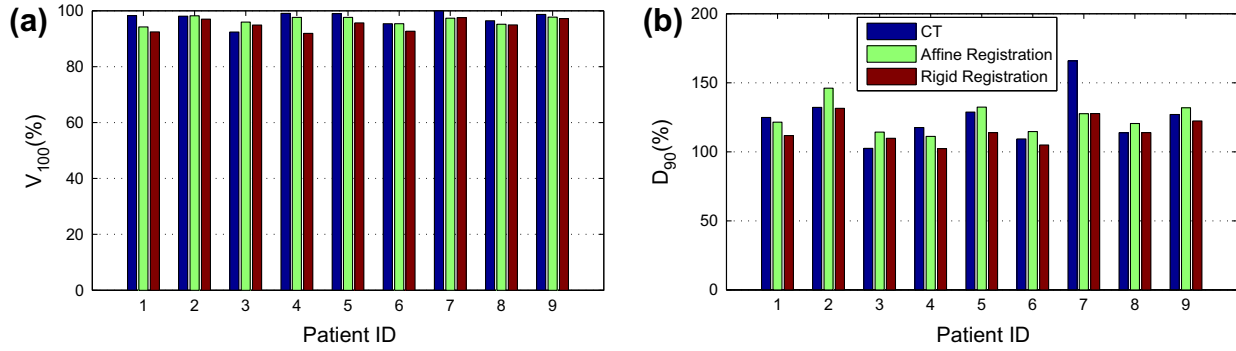
Fig. 9. (a) Volume of the prostate covered with 100% of the prescribed dose. (b) Dose delivered to the 90% of the prostate volume. V_{100} is shown in percentage of prostate volume and D_{90} is shown in percentage of the prescribed dose.

Table 4
Comparison of dosimetric parameters predicted using affine and rigid ultrasound–fluoroscopy registration versus Day-1 CT-based parameters.

Parameter	Method	N	Mean ± SD (%)	Range (%)	Prediction error Mean ± SD (%)	Ratio to CT Mean ± SD
V_{100}	CT	9	97.5 ± 2.4	92.4–99.9		
	R-UF	9	94.9 ± 2.2	91.9–97.5	3.1 ± 2.1	0.97 ± 0.03
	A-UF	9	96.6 ± 1.4	94.2–98.2	1.7 ± 1.4	0.99 ± 0.02
D_{90}	CT	9	124.6 ± 18.3	102.5–165.8		
	R-UF	9	115.3 ± 9.9	102.3–131.5	10.9 ± 11.7	0.93 ± 0.09
	A-UF	9	124.4 ± 11.2	111.1 – 146.1	10.5 ± 11.0	1.01 ± 0.11

R-UF: rigid ultrasound–fluoroscopy registration. A-UF: affine ultrasound–fluoroscopy registration.

3.4. Threshold parameter

The threshold parameter α in (1) plays an important role in the registration algorithm. If this parameter is too small, the thresholded image contains too many bright regions, most of which are false positives. In this case, the optimization algorithm may become trapped in local optima. On the other hand, if α is too large, many of the seeds are removed in the thresholded image, and then there may not be enough seeds present in the image to guide the optimizer. The threshold parameter could be determined based on the statistical properties of the ultrasound image. However, during our study on the phantom and all the clinical data sets, we used a fixed value of $\alpha = 2.5$. In order to study the performance of our algorithm over a range of values for α, the variation in the registration results were measured as follows.

Assume that $\mathbf{s}_{ij}$ represents the coordinates of the ith registered seed in the TRUS coordinate system, calculated using α_j, where $\alpha \in \{2, 2.5, 3\}$. Also assume that $\mathbf{m}_i$ is the average position of the ith seed over different values of α. Then $d_{ij} = \|\mathbf{s}_{ij} - \mathbf{m}_i\|$ represents

Table 5
Deviation of seed positions from the average position as a result of the change in α.

Patient ID	Deviation (mm) Mean ± SD
1	0.19 ± 0.08
2	0.26 ± 0.10
3	0.32 ± 0.12
4	0.33 ± 0.19
5	0.19 ± 0.08
6	0.25 ± 0.11
7	0.29 ± 0.14
8	0.18 ± 0.06
9	0.14 ± 0.05
10	0.18 ± 0.08
Overall	0.23 ± 0.13

the variation of a seed position with respect to its average position. Table 5 shows the mean and SD of the seed position variations caused by the changes in α. Our algorithm showed consistently successful registration for these different values of α. The sub-millimeter deviations in the seed positions demonstrate the robustness of our algorithm to variations in the threshold parameter and show that there is no need for fine-tuning.

4. Discussion

4.1. Accuracy in prediction of dose parameters

We compared our dosimetry results from ultrasound and fluoroscopy registration to postimplant CT dosimetry which, currently, is the standard quality assessment method. The comparison gives an overall accuracy assessment of our algorithm and shows its potential as a dynamic dosimetry system. The difference between our results and CT-based dosimetry can be caused by multiple factors as discussed below.

Su et al. (Su et al., 2007a) showed that seed localization uncertainties of less than 2 mm are expected to result in less than 5% error in D_{90}. As it can be seen in Table 2, the affine registration method resulted in a seed-to-seed registration error of less than 2 mm for all the patients. However, the dose parameters in Table 4 show average prediction errors of 10.9% and 10.5% calculated using the rigid and affine registration methods, respectively. It should be noted that in order to investigate the effects of seed localization uncertainties, Su et al. (Su et al., 2007a) added noise to the seed positions while keeping the prostate contours fixed. However, in our work, the dose parameters are calculated using prostate contours delineated in two different modalities—CT and ultrasound. CT imaging provides excellent visualization of the implanted seeds. However, soft tissue is not highly differentiated in this modality and thus, prostate contours delineated in CT can be different from prostate contours delineated in ultrasound. Lindsay et al. (Lindsay

et al., 2003) showed that the uncertainties in the prostate contours affect the prediction accuracy of D_{90} as adversely as uncertainties in seed localization.

In addition, postimplant prostate swelling may continue overnight and may result in changes in both the seed positions and the prostate volume compared to the time when the C-arm and TRUS images were acquired. These changes may then yield a difference between the dose parameters computed using Day-1 CT and ultrasound–fluoroscopy registration. Thus, the dose parameters prediction error is a combination of inter-modality prostate contour variation, prostate swelling, and seed localization error. The seed localization error, itself, is a combination of seed reconstruction errors and registration errors. The error caused by overnight prostate swelling and seed motion can be decreased by using Day-0 CT instead of Day-1 CT.

It is worth mentioning that a rigid registration between our reconstructed seeds and Day-1 CT seeds showed an average error of 1.8 ± 1.1 mm. Therefore, the effects of the differences between the prostate contours segmented in TRUS and CT seem to be more significant on the dose parameter prediction errors. The effect of prostate contouring errors on the dose prediction accuracy can be seen more vividly in patient 7 for whom, the error in the prediction of D_{90} is the greatest (see Fig. 9b). Note that, the prostate volume contoured in postimplant TRUS images for patient 7 is approximately 50% larger than the volume of the prostate contoured in CT (See Fig. 8). This is an indication of large prostate contouring error. If the data pertaining to this patient is removed as an outlier, the predication error for D_{90} is decreased to $7.5 \pm 6.2\%$ and $7.0 \pm 3.8\%$ for the rigid and affine registration methods, respectively. It should be mentioned that due to the presence of the seeds, prostate delineation in postimplant TRUS is difficult as well. Preoperative prostate contours are usually segmented right before the operation for intraoperative preplanning and can be used for calculation of dose parameters, although they do not account for intraoperative prostate swelling and motion. If the error between the preoperative prostate contours and the real prostate is large at the end of the operation, the brachytherapist can delineate the prostate again to calculate the dosimetry parameters with higher accuracy.

However, we should emphasize that the main purpose of dynamic dosimetry is to assure that the prostate is fully covered by the prescribed dose, while the patient is still in the treatment position. The isodose curves can be calculated, intraoperatively, using the registered seeds and overlaid on the real-time TRUS images. The physicians can use the isodose curves to conduct the procedure based on the real prostate boundaries visible in TRUS images, without a need for intraoperative prostate delineation.

4.2. Affine vs. rigid registration method

As Table 2 shows, the affine registration method with an average registration error of less than 2 mm for all the patients, shows better results compared to the rigid registration in term of seed-to-seed distances. As expected, the seed-to-seed distances differ most significantly along the y axis, since the affine registration method uses a scale along the y axis only. Fig. 6 demonstrates the importance of using an affine registration to reduce the effects of probe pressure.

The affine registration method resulted in a smaller average error in prediction of V_{100} compared to the rigid registration method (see Table 4). It also resulted in a less than 5% error in prediction of V_{100} for all the nine patients, while the rigid registration showed the same level of error only for seven of the patients. However, the prediction error in V_{100} is less than 10% for all the patients regardless of the registration method. Both rigid and affine registration methods resulted in approximately equivalent average pre-

diction errors for D_{90}. However, this error is less than 10% in six patients for the affine registration method compared to five patients for the rigid registration method.

In this work we used a 1D scaling to compensate for prostate deformation caused by the probe pressure. Our results show that this model was sufficiently accurate for the range of prostate volumes and probe pressures in this study. If the deformation is significantly larger due to excessive probe pressure applied by the physician or larger prostate volume, more sophisticated algorithms may be necessary. For example, a statistical analysis on a large patient data set can be used to identify major modes of deformation. Then, larger deformations can be compensated by adding the weight parameters of the deformation modes to the optimization loop. However, Wallner et al. (Wallner et al., 2001) indicated that one can achieve good acoustic coupling by gently pressing the probe against the prostate; therefore, excessive pressure should be avoided. Moreover, they argue that due to stiffness of the prostate, warping of the prostate in the US images at extreme pressures is caused by image artifact and not prostate deformation (Wallner et al., 2001). The prostate volumes in this study were 20.6–54.3 cc in postoperative CT. When the prostate volume is greater than 60 cc, the pubic arch interference becomes a concern (Davis et al., 2012). In our clinic, patients with prostate volumes greater than 55 cc are usually given a short course of androgen deprivation therapy to shrink their prostate.

4.3. Initialization

A good initial estimate of the registration parameters plays an important role in the convergence of the algorithm to the global optimum. In this work, we initialized the rotational parameters using the planned position of the seeds. We also initialized the translational parameters so that the center of mass of the seeds coincides with the center of the VOI. This initialization resulted in convergence of our algorithm to below 2 mm registration error for all the patients without a need to restart the algorithm from different initial guesses.

If the algorithm is used intraoperatively, when only a partial set of the seeds are implanted, coinciding the center of mass of the implanted seeds with the center of mass of the planned seeds up to that stage can provide a good initial estimate for the translational parameters. The same method can be used to initialize the rotational parameters. Due to high computational speed of our algorithm, the registration can be restarted from different initial estimates if a failure occurs.

We expect our algorithm to show successful results when a large portion of the seeds are implanted. However, rigorous evaluation of our work in cases that a small number of seeds are implanted is subject of future work.

5. Conclusions and future work

In this paper, we introduced a new nonrigid image-based ultrasound–fluoroscopy registration method to provide a practical solution for dynamic dosimetry in prostate brachytherapy. We employed thresholding and Gaussian blurring to enhance the quality of the TRUS images and prepare them for registration. We used a computationally efficient point-to-volume similarity metric and a stochastic evolutionary optimizer within our registration loop.

Our trials on a ground truth phantom showed registration errors of 0.84 ± 0.45 mm (mean ± SD) for initial alignment errors of ± 15 mm along each axis and $\pm 15°$ around each axis, despite the presence of false positives and missing seeds. In a trial on 10 patient data sets, our algorithm achieved overall registration errors of 1.5 ± 0.9 mm and 1.7 ± 1.0 mm for the affine and rigid registrations, respectively. The affine registration method succeeded in

achieving an average registration error of less than 2 mm for all the patients. In a dosimetry comparison with Day-1 CT for 9 patients, our registration results showed prediction errors of $3.11 \pm 2.06\%$ and $1.70 \pm 1.42\%$ for V_{100} in rigid and affine modes, respectively. It also showed prediction errors of $10.9 \pm 11.7\%$ and $10.5 \pm 11.0\%$ for D_{90} in rigid and affine modes, respectively, which were decreased to $7.5 \pm 6.2\%$ and $7.0 \pm 3.8\%$, after removal of an outlier.

In summary, our image-based ultrasound–fluoroscopy registration method is capable of providing accurate registration and dosimetry results within a clinically acceptable time frame. In contrast to previous work, it is able to account for prostate motion and deformation caused by the probe retraction and also perform the registration without a need for manual seed segmentation. Considering the results, our algorithm is a promising method for providing dynamic dosimetry and improving prostate brachytherapy treatment quality.

Investigation on performance of the algorithm in clinical setting and comparison to Day-0 CT are part of the future work.

Acknowledgments

References

Amols, H.I., Rosen, I.I., 1981. A three-film technique for reconstruction of radioactive seed implants. Med. Phys. 8 (2), 210–214.

Blasko, J.C., Mate, T., Sylvester, J.E., Grimm, P.D., Cavanagh, W., 2002. Brachytherapy for carcinoma of the prostate: techniques, patient selection, and clinical outcomes. Semin. Radiat. Oncol. 12 (1), 81–94. Advances in Brachytherapy.

Brunet-Benkhoucha, M., Verhaegen, F., Reniers, B., Lassalle, S., Béliveau-Nadeau, D., Donath, D., Taussky, D., Carrier, J.-F., 2009. Clinical implementation of a digital tomosynthesis-based seed reconstruction algorithm for intraoperative postimplant dose evaluation in low dose rate prostate brachytherapy. Med. Phys. 36 (11), 5235–5244.

Chen, T.K., Thurston, A.D., Ellis, R.E., Abolmaesumi, P., 2009. A real-time freehand ultrasound calibration system with automatic accuracy feedback and control. Ultrasound Med. Biol. 35 (1), 79–93.

Davis, B.J., Horwitz, E.M., Lee, W.R., Crook, J.M., Stock, R.G., Merrick, G.S., Butler, W.M., Grimm, P.D., Stone, N.N., Potters, L., Zietman, A.L., Zelefsky, M.J., 2012. American brachytherapy society consensus guidelines for transrectal ultrasound-guided permanent prostate brachytherapy. Brachytherapy 11 (1), 6–19.

Dehghan, E., Jain, A.K., Moradi, M., Wen, X., Morris, W.J., Salcudean, S.E., Fichtinger, G., 2011a. Brachytherapy seed reconstruction with joint-encoded C-arm single-axis rotation and motion compensation. Med. Image Anal. 15 (5), 760–771.

Dehghan, E., Lee, J., Fallavollita, P., Kuo, N., Deguet, A., Burdette, E.C., Song, D., Prince, J.L., Fichtinger, G., 2011b. Point-to-volume registration of prostate implants to ultrasound. In: Proc. Medical Image Computing and Computer Assisted Intervention (MICCAI).

Dehghan, E., Moradi, M., Wen, X., French, D., Lobo, J., Morris, W.J., Salcudean, S.E., Fichtinger, G., 2011c. Prostate implant reconstruction from C-arm images with motion-compensated tomosynthesis. Med. Phys. 38 (10), 5290–5302.

Ding, M., Wei, Z., Gardi, L., Downey, D.B., Fenster, A., 2006. Needle and seed segmentation in intra-operative 3D ultrasound-guided prostate brachytherapy. Ultrasonics 44 (Suppl. 1), e331–e336, Proceedings of Ultrasonics International (UI'05) and World Congress on Ultrasonics (WCU).

Fallavollita, P., Karim-Aghaloo, Z., Burdette, E., Song, D., Abolmaesumi, P., Fichtinger, G., 2010. Registration between ultrasound and fluoroscopy or CT in prostate brachytherapy. Med. Phys. 37 (6), 2749–2760.

Feleppa, E.J., Ramachandran, S., Alam, S.K., Kalisz, A., Ketterling, J.A., Ennis, R.D., Wuu, C.-S., 2002. Novel methods of analyzing radio-frequency echo signals for the purpose of imaging brachytherapy seeds used to treat prostate cancer. In: Proc SPIE, vol. 4687, pp. 127–138.

French, D.F., Morris, J., Keyes, M., Goksel, O., Salcudean, S.E., 2005. Intraoperative dosimetry for prostate brachytherapy from fused ultrasound and fluoroscopy images. Acad. Radiol. 12 (10), 1262–1272.

Han, B.H., Wallner, K., Merrick, G., Butler, W., Sutlief, S., Sylvester, J., 2003. Prostate brachytherapy seed identification on post-implant TRUS images. Med. Phys. 30 (5), 898–900.

Hansen, N., 2006. The CMA evolution strategy: a comparing review. In: Lozano, J.A., Larranaga, P., Inza, I., Bengoetxea, E. (Eds.), Towards a New Evolutionary Computation. Advances on Estimation of Distribution Algorithms, Studies in Fuzziness and Soft Computing, vol. 192. Springer, Berlin/Heidelberg, pp. 75–102.

Holmes III, D.R., Robb, R.A., 2004. Improved automated brachytherapy seed localization in trans-urethral ultrasound data. In: Galloway, R.L. (Ed.), Proc. SPIE, vol. 5367, pp. 353–360.

Jain, A., Deguet, A., Iordachita, I., Chintalapani, G., Vikal, S., Blevins, J., Le, Y., Armour, E., Burdette, C., Song, D., Fichtinger, G., 2012. Intra-operative 3D guidance and edema detection in prostate brachytherapy using a non-isocentric C-arm. Med. Image Anal. 16 (3), 731–743.

Jain, A.K., Mustufa, T., Zhou, Y., Burdette, C., Chirikjian, G.S., Fichtinger, G., 2005a. FTRAC – a robust fluoroscope tracking fiducial. Med. Phys. 32 (10), 3185–3198.

Jain, A.K., Zhou, Y., Mustufa, T., Burdette, C., Chirikjian, G.S., Fichtinger, G., 2005b. Matching and reconstruction of brachytherapy seeds using the Hungarian algorithm (MARSHAL). Med. Phys. 32 (11), 3475–3492.

Kuo, N., Deguet, A., Song, D.Y., Burdette, E.C., Prince, J.L., Lee, J., 2012. Automatic segmentation of radiographic fiducial and seeds from x-ray images in prostate brachytherapy. Med. Eng. Phys. 34 (1), 64–77.

Lagerburg, V., Moerland, M.A., Lagendijk, J.J., Battermann, J.J., 2005. Measurement of prostate rotation during insertion of needles for brachytherapy. Radiother. Oncol. 77 (3), 318–323.

Lam, S.T., Cho, P.S., Marks II, R.J., Narayanan, S., 2004. Three-dimensional seed reconstruction for prostate brachytherapy using Hough trajectories. Phys. Med. Biol. 49 (4), 557–569.

Lee, J., Kuo, N., Deguet, A., Dehghan, E., Song, D.Y., Burdette, E.C., Prince, J.L., 2011a. Intraoperative 3D reconstruction of prostate brachytherapy implants with automatic pose correction. Phys. Med. Biol. 56 (15), 5011–5027.

Lee, J., Labat, C., Jain, A.K., Song, D.Y., Burdette, E.C., Fichtinger, G., Prince, J.L., 2011b. REDMAPS: reduced-dimensionality matching for prostate brachytherapy seed reconstruction. IEEE Trans. Med. Imag. 30 (1), 38–51.

Lee, J., Liu, X., Jain, A., Song, D., Burdette, E., Prince, J., Fichtinger, G., 2009. Prostate brachytherapy seed reconstruction with Gaussian blurring and optimal coverage cost. IEEE Trans. Med. Imag. 28 (12), 1955–1968.

Lindsay, P.E., Van Dyk, J., Battista, J.J., 2003. A systematic study of imaging uncertainties and their impact on ^{125}I prostate brachytherapy dose evaluation. Med. Phys. 30 (7), 1897–1908.

McAleavey, S., Rubens, D., Parker, K., 2003. Doppler ultrasound imaging of magnetically vibrated brachytherapy seeds. IEEE Trans. Biomed. Eng. 50 (2), 252–254.

Meijer, G.J., van den Berg, H.A., Hurkmans, C.W., Stijns, P.E., Weterings, J.H., 2006. Dosimetric comparison of interactive planned and dynamic dose calculated prostate seed brachytherapy. Radiother. Oncol. 80 (3), 378–384.

Merrick, G.S., Butler, W.M., Lief, J.H., Dorsey, A.T., 2001. Is brachytherapy comparable with radical prostatectomy and external-beam radiation for clinically localized prostate cancer? Tech. Urol. 7 (1), 12–19.

Mitri, F., Trompette, P., Chapelon, J.-Y., 2004. Improving the use of vibro-acoustography for brachytherapy metal seed imaging: a feasibility study. IEEE Trans. Med. Imag. 23 (1), 1–6.

Morris, W., Keyes, M., Palma, D., Spadinger, I., McKenzie, M., Agranovich, A., Pickles, T., Liu, M., Kwan, W., Wu, J., Berthelet, E., Pai, H., 2009. Population-based study of biochemical and survival outcomes after permanent ^{125}I brachytherapy for low- and intermediate-risk prostate cancer. Urology 73 (4), 860–865.

Nag, S., Ciezki, J.P., Cormak, R., Doggett, S., Dewyngaert, K., Edmundson, G.K., Stock, R.G., Stone, N.N., Yan, Y., Zelefsky, M.J., 2001. Intraoperative planning and evaluation of permanent prostate brachytherapy: report of the American brachytherapy society. Int. J. Radiat. Oncol. Biol. Phys. 51 (5), 1422–1430.

Narayanan, S., Cho, P.S., Marks II, R.J., 2004. Three-dimensional seed reconstruction from an incomplete data set for prostate brachytherapy. Phys. Med. Biol. 49 (15), 3483–3494.

Nath, R., Bice, W.S., Butler, W.M., Chen, Z., Meigooni, A.S., Narayana, V., Rivard, M.J., Yu, Y., 2009. AAPM recommendations on dose prescription and reporting methods for permanent interstitial brachytherapy for prostate cancer: report of task group 137. Med. Phys. 36 (11), 5310–5322.

Nath, S., Chen, Z., Yue, N., Trumpore, S., Peschel, R., 2000. Dosimetric effects of needle divergence in prostate seed implant using I125 and Pd103 radioactive seeds. Med. Phys. 27 (5), 1058–1066.

Orio III, P.F., Tutar, I.B., Narayanan, S., Arthurs, S., Cho, P.S., Kim, Y., Merrick, G., Wallner, K.E., 2007. Intraoperative ultrasound–fluoroscopy fusion can enhance prostate brachytherapy quality. Int. J. Radiat. Oncol. Biol. Phys. 69 (1), 302–307.

Polo, A., Salembier, C., Venselaar, J., Hoskin, P., 2010. Review of intraoperative imaging and planning techniques in permanent seed prostate brachytherapy. Radiother. Oncol. 94 (1), 12–23.

Potters, L., Calguaru, E., Thornton, K.B., Jackson, T., Huang, D., 2003. Toward a dynamic real-time intraoperative permanent prostate brachytherapy methodology. Brachytherapy 2 (3), 172–180.

Rivard, M.J., Coursey, B.M., DeWerd, L.A., Hanson, W.F., Huq, M.S., Ibbott, G.S., Mitch, M.G., Nath, R., Williamson, J.F., 2004. Update of AAPM Task Group No.43 Report: a revised AAPM protocol for brachytherapy dose calculations.. Med. Phys. 31 (3), 633–674.

Siegel, R., Ward, E., Brawley, O., Jemal, A., 2011. Cancer statistics, 2011. CA: Cancer J. Clin. 61 (4), 212–236.

Song, D.Y., Jain, A.K., Zhang, Z., Deguet, A., Le, Y., Armour, E., Burdette, E.C., Fichtinger, G., 2011. Dynamic intraoperative dosimetry for prostate brachytherapy using a nonisocentric C-arm. Brachytherapy 10 (2), 98–106.

Su, Y., Davis, B.J., Furutani, K.M., Herman, M.G., Robb, R.A., 2007a. Dosimetry accuracy as a function of seed localization uncertainty in permanent prostate brachytherapy: increased seed number correlates with less variability in prostate dosimetry. Phys. Med. Biol. 52 (11), 3105–3119.

Su, Y., Davis, B.J., Furutani, K.M., Herman, M.G., Robb, R.A., 2007b. Seed localization and TRUS-fluoroscopy fusion for intraoperative prostate brachytherapy dosimetry. Comput. Aid. Surg. 12 (1), 25–34.

Su, Y., Davis, B.J., Herman, M.G., Robb, R.A., 2004. Prostate brachytherapy seed localization by analysis of multiple projections: identifying and addressing the seed overlap problem. Med. Phys. 31 (5), 1277–1287.

Todor, D.A., Zaider, M., Cohen, G.N., Worman, M.F., Zelefsky, M.J., 2003. Intraoperative dynamic dosimetry for prostate implants. Phys. Med. Biol. 48 (9), 1153–1171.

Tutar, I.B., Gong, L., Narayanan, S., Pathak, S.D., Cho, P.S., Wallner, K., Kim, Y., 2008. Seed-based transrectal ultrasound–fluoroscopy registration method for intraoperative dosimetry analysis of prostate brachytherapy. Med. Phys. 35 (3), 840–848.

Tutar, I.B., Narayanan, S., Lenz, H., Nurani, R., Orio, P., Cho, P.S., Wallner, K., Kim, Y., 2007. Seed-based ultrasound and fluoroscopy registration using iterative optimal assignment for intraoperative prostate brachytherapy dosimetry. In: Proc. SPIE.

Wallner, K., Blasko, J.C., Dattoli, M., 2001. Prostate Brachytherapy Made Complicated, second ed. Smartmedicine Press.

Wei, Z., Gardi, L., Downey, D.B., Fenster, A., 2006. Automated localization of implanted seeds in 3D TRUS images used for prostate brachytherapy. Med. Phys. 33 (7), 2404–2417.

Wen, X., Salcudean, S.E., Lawrence, P.D., 2010. Detection of brachytherapy seeds using 3D transrectal ultrasound. IEEE Trans. Biomed. Eng. 57 (10), 2467–2477.

Xue, J., Waterman, F., Handler, J., Gressen, E., 2005. Localization of linked 125I seeds in postimplant trus images for prostate brachytherapy dosimetry. Int. J. Radiat. Oncol. Biol. Phys. 63 (Suppl. 1), S522–S523.

Yamada, Y., Potters, L., Zaider, M., Cohen, G., Venkatraman, E., Zelefsky, M.J., 2003. Impact of intraoperative edema during transperineal permanent prostate brachytherapy on computer-optimized and preimplant planning techniques. Am. J. Clin. Oncol. 26 (5), e130–e135.